Mixing Driven by Radiative and Evaporative Cooling at the Stratocumulus Top

ALBERTO DE LOZAR AND JUAN PEDRO MELLADO

Max Plank Institute for Meteorology, Hamburg, Germany

(Manuscript received 19 March 2015, in final form 16 July 2015)

ABSTRACT

The stratocumulus-top mixing process is investigated using direct numerical simulations of a shear-free cloud-top mixing layer driven by evaporative and radiative cooling. An extension of previous linear formulations allows for quantifying radiative cooling, evaporative cooling, and the diffusive effects that artificially enhance mixing and evaporative cooling in high-viscosity direct numerical simulations (DNS) and many atmospheric simulations. The diffusive cooling accounts for 20% of the total evaporative cooling for the highest resolution (grid spacing ~14 cm), but this can be much larger (~100%) for lower resolutions that are commonly used in large-eddy simulations (grid spacing ~5 m). This result implies that the κ scaling for cloud cover might be strongly influenced by diffusive effects. Furthermore, the definition of the inversion point as the point of neutral buoyancy $\langle b \rangle(z_i) = 0$ allows the derivation of two scaling laws. The in-cloud scaling law relates the velocity and buoyancy integral scales to a buoyancy flux defined by the inversion point. The entrainment-zone scaling law provides a relationship between the entrainment velocity and the liquid evaporation rate. By using this inversion point, it is shown that the radiative-cooling contribution to the entrainment velocity decouples from the evaporative-cooling contribution and behaves very similarly as in the smoke cloud. Finally, evaporative and radiative cooling have similar strengths, when this strength is measured by the integrated buoyancy source. This result partially explains why current entrainment parameterizations are not accurate enough, given that most of them implicitly assume that only one of the two mechanisms rules the entrainment.

1. Introduction

Since the seminal work of Lilly (1968), the parameterization of the entrainment velocity in stratocumulus remains a challenge. The uncertainty in the entrainment velocity remains of order one in measurements (Faloona et al. 2005; Gerber et al. 2013) as well as in numerical simulations (Stevens 2005). This uncertainty complicates an accurate parameterization of stratocumulus clouds in climate models and numerical weather prediction models (Stevens 2002).

Most difficulties for accurately resolving entrainment processes in numerical simulations stem from the large separation of scales between the large-scale convective motions of the stratocumulus-topped boundary layer (STBL) and the length scales that control the entrainment process. The separation of scales originates from the strong stratification capping the STBL, which imposes a limitation on the size of the eddies that directly contribute to the entrainment process. As a result, the entrainment zone, loosely defined as the region where the entrainment happens, is much thinner than the STBL [~10–60 m as estimated by Haman (2009) and Gerber et al. (2013)]. The challenge is to represent at the same time the effect of the scales that are relevant for the entrainment and the larger-scale flow that characterizes the STBL.

Large-eddy simulations (LES) of the STBL typically focus on solving the large-scale processes and cannot fully resolve entrainment processes, which are partly accounted for by the subgrid model. To complement LES by focusing more on the small scales, Mellado et al. (2009) introduced the cloud-top mixing-layer configuration: two horizontally spread layers that represent the cloud top and the free atmosphere above. Studies in a cloud-top mixing layer investigate how different cloud forcings generate entrainment, while neglecting other processes and couplings that might be important for the STBL dynamics on a longer time scale. These studies aim to resolve the length scales that are directly relevant for entrainment, which can be accomplished by using direct numerical simulations (DNS).

Corresponding author address: Alberto de Lozar, Max Plank Institute for Meteorology, Bundestr. 53, 20146 Hamburg, Germany. E-mail: adelozar@gmail.com

DOI: 10.1175/JAS-D-15-0087.1

Past studies in a cloud-top mixing layer have shown that evaporative cooling alone cannot generate significant entrainment (Mellado et al. 2009; Mellado 2010), unless acting in combination with other mechanisms like a strong enough shear at the cloud top (Mellado et al. 2014). At the same time, evaporative cooling produces very weak in-cloud turbulence, even for the strong shear cases. On the other hand, De Lozar and Mellado (2013) have shown that radiative cooling alone in a so-called smoke cloud produces a reasonable intensity of in-cloud turbulence, but the entrainment velocities are 50% below the measured values.

In this paper, we investigate the combined effect of radiative and evaporative cooling in a cloud-top mixing-layer configuration using DNS. We aim to develop generic scaling laws that can help to derive entrainment-velocity parameterizations. In section 2 we describe the linearized formulation that we use in this paper and the consequences of this approximation. Section 3 is dedicated to the description of the simulation setup and the numerical experiments. In section 4 we investigate the evaporative-cooling buoyancy source and quantify the diffusive entrainment that appears as a result of a too-high viscosity. In section 5, we define an inversion point that divides the cloud from the entrainment zone and justify this choice by showing the validity of two scaling laws that are consistent with this definition. The first scaling law characterizes the in-cloud flow. The second scaling law relates the total evaporative cooling to the entrainment velocity. The turbulent and direct cooling contributions to the entrainment velocity that stem from the definition of the inversion point are presented in section 6. Section 7 describes the implications of this study for LES and for entrainment parameterizations. Finally, we present our conclusions in section 8.

2. Formulation

a. The linearized formulation

The formulation is based on the set of equations presented in Mellado et al. (2010) and De Lozar and Mellado (2014), which has been extended to retain the effect of radiative cooling. The formulation is based on two conserved variables: total water q_t and enthalpy h. Following Albrecht et al. (1985) the total water is expressed by a mixing fraction χ:

$$q_t = q_t^c + (q_t^d - q_t^c)\chi, \tag{1}$$

where the superscripts c and d refer to two reference states in the cloud and dry free atmosphere. The enthalpy is expressed as

$$h = h^c + (h^d - h^c)\chi + \psi, \tag{2}$$

where ψ represents the deviations from the linear mixing line due to radiative cooling. The two reference states describe the two layers that form a cloud-top mixing-layer configuration. The top, dry layer is given by the combination ($\chi = 1$ and $\psi = 0$) and the cloud, bottom layer by ($\chi = 0$ and $\psi = 0$).

The evolution equations are written in the Boussinesq approximation for the case that all diffusion coefficients are equal to the thermal diffusivity:

$$\begin{aligned} d\mathbf{u}/dt &= -\boldsymbol{\nabla} p + \nu\nabla^2\mathbf{u} + b\mathbf{k}, \\ d\chi/dt &= \kappa_T\nabla^2\chi, \quad \text{and} \\ d\psi/dt &= \kappa_T\nabla^2\psi - r, \end{aligned} \tag{3}$$

where $d/dt = \partial/\partial t + \mathbf{u}\cdot\boldsymbol{\nabla}$ is the material derivative, ν is the kinematic viscosity, and κ_T is the thermal diffusivity. In this study we assume that the Prandtl number is equal to one: $\mathrm{Pr} = \nu/\kappa_T = 1$.

The radiative cooling is described by a one-dimensional radiation scheme:

$$r = F_0(\lambda\rho)^{-1}\ell\cdot\exp\left[-\lambda^{-1}\int_z^{z_{\mathrm{top}}}\ell(z')\,dz'\right], \tag{4}$$

where $\ell = q_1/q_1^c$ is the normalized liquid water. The radiation scheme assumes that longwave radiation only propagates in the vertical direction. The resulting radiative forcing is defined by the total cooling per unit area F_0 and by the extinction length λ that defines the region where the radiative cooling is effective (Larson et al. 2007; De Lozar and Mellado 2013).

The buoyancy and liquid-water equations are simplified in a procedure similar to Bretherton (1987) and Pauluis and Schumacher (2010), which is detailed in the appendix. The main simplifications are the assumption of infinitely fast thermodynamics and the linearization of the buoyancy and saturated-vapor content equations. In our reference case these simplifications introduce only a small error in the buoyancy b of around 3% with respect to the full formulation. The resulting forms for the liquid water and buoyancy read as follows:

$$\begin{aligned} \ell &= f(\xi) = \epsilon\ln[\exp(\xi/\epsilon) + 1] \quad \text{and} \\ b/\Delta b &= \chi\left(\frac{1+D}{1-\chi_s}\right) + \frac{\psi}{\psi_b} + (\ell - 1)\left(\frac{D+\chi_s}{1-\chi_s}\right), \end{aligned} \tag{5}$$

where $\Delta b = b^d - b^c$, and the variable

$$\xi = 1 - \chi/\chi_s - \psi/\psi_s \tag{6}$$

defines the cloud–dry air boundary by $\xi = 0$. The function $f(\xi)$ tends to the piecewise linear function defined

by Bretherton (1987) in the limit $\epsilon \to 0$, but it has a finite second-order derivative. Mellado et al. (2009) showed that when $\epsilon \leq 1/16$ the results become independent of ϵ and tend to the piecewise linear limit. Consequently, we use $\epsilon = 1/16$. In the absence of radiative cooling ($r = 0$) $\psi \to 0$, and the set of equations for the mixing line formulation is recovered. In this limit, $D = -b_s/\Delta b$ is the normalized buoyancy of the just saturated (no liquid) cloud–dry air mixture, which occurs at the mixing ratio $\chi = \chi_s$. The parameters D and χ_s fully characterize the buoyancy reversal instability (BRI), which happens for the condition $D > 0$ (Siems and Bretherton 1992; Mellado et al. 2009). The parameters ψ_b and ψ_s scale how the variations in enthalpy, given by ψ in Eq. (2), modify the nondimensional buoyancy and liquid water, respectively. In the appendix the parameters D, χ_s, ψ_s, and ψ_b are given as functions of the inversion properties.

b. Nondimensionalization

Once the initial conditions are sufficiently forgotten, dimensional analysis shows that the cloud-top mixing-layer flow properties depend only on the height z, the mixing-layer depth z^*, and on five nondimensional numbers. Our choice of nondimensional numbers is

$$\{\mathrm{Ri}_0, \mathrm{Re}_0, D, \chi_s, \beta\}. \tag{7}$$

This set is an extended version of the set that we used in the radiative-cooling-only case (De Lozar and Mellado 2013). The nondimensionalization is based on the parameters imposed by the radiative forcing: the reference buoyancy flux $B_0 = (F_0 g)/(\rho c_{p,0} T_c)$ and the length scale λ. These parameters define a reference velocity and buoyancy scale: $U_0 = (B_0 \lambda)^{1/3}$ and $b_0 = B_0/U_0$, which can be used to construct a reference Richardson number $\mathrm{Ri}_0 = \Delta b/b_0$ and a reference Reynolds number $\mathrm{Re}_0 = U_0 \lambda/\nu$. The reference Richardson number characterizes the strength of the inversion against eddies of size λ, and it is much larger than typical gradient Richardson numbers observed in stratocumulus (Katzwinkel et al. 2012). The reference Reynolds number characterizes the diffusive effects and the separation of scales in the entrainment zone (which is typically of order λ). The parameters D and χ_s fully describe the evaporative cooling in the mixing line formulation (Siems and Bretherton 1992) and have been introduced in section 2a. Finally, the parameter β (defined in the appendix) relates the changes of buoyancy to the variations in enthalpy within saturated layers and plays the same role as the parameter β in Randall (1980) or as the parameter a_{sat} in van Zanten and Duynkerke (2002).

c. Isobaric mixing in the linearized formulation

The linear approximations combined with infinitely fast thermodynamics impose a constraint for isobaric mixing: net evaporation of droplets is only possible through mixing of saturated and unsaturated parcels, as typically happens at the cloud top. By net evaporation, we mean a process in which the volume-integrated liquid-water content decreases when mixing two parcels of fixed size. This limitation originates from writing the saturated-water content at constant pressure q_s as a linear combination of the conserved variables h and q_t. This implies that the saturated-water content also behaves as a conserved variable for isobaric mixing processes. In the infinitely fast thermodynamics approximation the liquid water content in saturated parcels is given by $q_l = q_t - q_s$, which is also a linear function of the conserved variables. As a result, the liquid water behaves as a conserved variable when mixing two saturated parcels, and the volume-integrated liquid water content stays constant. This result is used to justify the entrainment scaling presented in section 5.

A corollary of the previous statement is that it is not possible to obtain net condensation of droplets through isobaric mixing in the linear approximation. In unsaturated parcels the total water content is below the saturated water content; that is, $q_t < q_s$. Since q_t and q_s mix linearly as conserved scalars, it is not possible to mix two unsaturated parcels resulting in a saturated parcel such that $q_t > q_s$.

3. Simulations setup

a. Flow scales in a cloud-top mixing layer

In our simulations we aim to resolve the length scales that are relevant for the interaction of evaporative and radiative cooling with the inversion dynamics. The scale relevant for radiative cooling is the depth of the region cooled by longwave radiation—that is, the extinction length λ, which has a typical value of $\simeq$15 m. The evaporative cooling is determined by molecular mixing, and hence it is directly related to the entrainment process. De Lozar and Mellado (2013) found that the turbulent flux of buoyancy in the entrainment zone can be related to eddies between 50 cm and 60 m, suggesting that the relevant scales for entrainment are also around this interval. This assumption is also supported by measurements of the entrainment mass flux in the POST campaign, which are related to roughly the same range of scales (Gerber et al. 2013). We conclude that the set of the relevant scales that need to be resolved is also approximately centered around λ.

We have to assess the relevance for our problem of the atmospheric scales that we do not retain in the analysis.

The smallest resolved scale in DNS is on the order of the Kolmogorov length, which is estimated by assuming that buoyancy production balances the dissipation of turbulent kinetic energy: $\eta \simeq \nu^{3/4} B_0^{-1/4}$. The separation of scales between our reference scale λ and the Kolmogorov length is then estimated from our definition of the reference Reynolds number: $\mathrm{Re}_0 \simeq (\lambda/\eta)^{4/3}$. In atmospheric flows the Kolmogorov length is around $\eta_{\mathrm{at}} \sim 1\,\mathrm{mm}$, and the corresponding Reynolds number $\mathrm{Re}_0 \sim 10^5$ is currently inaccessible for DNS. To resolve length scales comparable to the radiation scale, the Kolmogorov scale is adjusted by increasing the viscosity of the fluid to values that are much higher than in air, so that $\eta \sim 10\,\mathrm{cm}$ and $\mathrm{Re}_0 \sim 10^3$. This procedure effectively neglects all flow scales between the atmospheric Kolmogorov length and the Kolmogorov length in the simulation. We assume that flow statistics can be extrapolated to the atmospheric conditions when they become independent of the smallest resolved length scales in the simulations—that is, when they become independent of Re_0 (Monin and Yaglom 1971; Dimotakis 2005). The Re_0 independency is tested by performing several simulations with different Re_0. This test is important because an enhanced viscosity might affect the flow in ways that are different to just the dissipation of the neglected small scales, as it is shown in section 4.

The largest scale of the flow in a cloud-top mixing layer is on the order of the integral length scale z^* (defined in section 5), which is proportional to the mixing-layer depth. In our configuration this depth grows continuously with time so that the dependence on the largest scales of the flow (or z^*) is translated to a time dependence. When the mixing layer is capped by a stratification, we can expect that some entrainment-zone properties become eventually independent of z^* because large eddies cannot directly generate entrainment [see, e.g., Fernando (1991) and references therein]. This expectation is based on the scale separation between the small-scale entrainment eddies and z^*, when z^* is large enough. The condition of being independent of z^* also indicates that other large-scale processes, not modeled in the cloud-top mixing layer, cannot interact directly with the entrainment eddies and will not affect the entrainment directly on a short-time scale. On a longer time scale, large-scale processes can modify the entrainment through the variation of the mean properties of the cloud (like the cloud moistening due to the surface fluxes or large-scale subsidence) or through the variation of the input of kinetic energy that receives the entrainment eddies via the turbulent cascade (like the enhancement in kinetic energy due to surface fluxes or cloud-base heating).

Finally, the total separation of scales inside the cloud [estimated by $\mathrm{Re}^* = w^* z^*/\nu \simeq (z^*/\eta)^{4/3} \sim 10^4$, where the integral velocity scale w^* is defined in section 5] is sufficiently high to expect Reynolds number independency in the second-order statistics we show in this paper (Monin and Yaglom 1971; Dimotakis 2005). Consistent with those values of Re^*, the Reynolds number based on the Taylor microscale Re_λ [as defined in Pope (2000) for example] is also sufficiently high in the cloud bulk $\mathrm{Re}_\lambda \sim 75$–$250$ and in the inversion layer $\mathrm{Re}_\lambda \sim 50$–$200$.

b. Simulation parameters

Our reference case is based on a nighttime flight RF-01 in unbroken stratocumulus of the DYCOMS-II campaign, as described in Stevens et al. (2005). We divide the simulations into three groups in Table 1. In the first group we include the simulations of the reference case, together with the cases in which we only vary the BRI parameter D. This study is the main focus of this paper, and therefore we have employed most of our computational time for the simulations of this group, often using broader domains in order to reach higher statistical convergence.

In the second group we perform two simulations in which all evaporative-cooling parameters are equal as in the reference simulation, but we decrease systematically the ratio of the stratification to the radiative cooling defined by Ri_0. This is equivalent to increasing the radiative forcing by a factor of 2 and 4 with respect to the reference case.

In the third group we explore the possibility of varying χ_s and D at the same time for a reduced number of cases. The last case of this group is based on measurements of Arctic stratocumulus from the reference flight 11 of the VERDI campaign (Klingebiel et al. 2015). The jump in humidity in VERDI ($\Delta q_t = -0.65\,\mathrm{g\,kg^{-1}}$) is considerably lower than in DYCOMS-II ($\Delta q_t = -7.5\,\mathrm{g\,kg^{-1}}$), whereas the longwave radiative properties are quite similar. Therefore, the relative importance of evaporative cooling over radiation in VERDI is expected to be considerably lower than in DYCOMS-II. The VERDI simulation is the only one in which we varied the parameter β in order to match the measured value.

We have explored the dependence on the unresolved small scales by performing four simulations with different Re_0 for the reference case. Additionally, simulations with two different Re_0 were performed for many other cases in the first and third group. The simulations with low Re_0 typically cover a wider range of z^* and were also used to explore the dependence on the large scales.

The largest length scale that is reached in each simulation is comparable to the mixing layer depth at the

TABLE 1. Parameters in the simulation. The first column contains the label of each simulation, where the group is given by the roman numbers. We have kept the same label for all simulations that only differ in the Reynolds number. The next columns present the parameters that define each simulation. The evaporative cooling is defined by the parameters D, χ_s, and β. The radiative cooling is defined by a reference Richardson number Ri_0, and the viscous forces are characterized by a reference Reynolds number Re_0. The seventh column indicates the vertically averaged buoyancy flux at the last time step $\mathcal{B} = (z^*)^{-1}\int \langle w'b' \rangle \, dz$, scaled by the radiative forcing. The eighth column shows the domain size in dimensions of the extinction length (typically $\lambda = 15$ m), differentiating between the horizontal and the vertical extension. The ninth column represents the number of points of the numerical grid. The last column indicates the cases that were motivated by in situ measurements (see text).

No.	D	χ_s	β	Ri_0	Re_0	$\mathcal{B}S_{\mathrm{rad}}^{-1}$	Domain size	Numerical grid	Campaign
Ia	−0.045	0.09	0.53	40	400	0.74	$(30\lambda)^2 \times 30\lambda$	$(1024)^2 \times 1024$	—
Ia	−0.045	0.09	0.53	40	800	0.79	$(36\lambda)^2 \times 18\lambda$	$(2048)^2 \times 1024$	—
Ib	0.031	0.09	0.53	40	200	1.30	$(50\lambda)^2 \times 50\lambda$	$(1024)^2 \times 1024$	DYCOMS-II
Ib	0.031	0.09	0.53	40	400	1.22	$(30\lambda)^2 \times 30\lambda$	$(1024)^2 \times 1024$	DYCOMS-II
Ib	0.031	0.09	0.53	40	800	1.18	$(36\lambda)^2 \times 18\lambda$	$(2048)^2 \times 1024$	DYCOMS-II
Ib	0.031	0.09	0.53	40	1600	1.16	$(27\lambda)^2 \times 18\lambda$	$(3072)^2 \times 2048$	DYCOMS-II
Ic	0.06	0.09	0.53	40	400	1.61	$(30\lambda)^2 \times 30\lambda$	$(1024)^2 \times 1024$	—
Ic	0.06	0.09	0.53	40	800	1.48	$(36\lambda)^2 \times 18\lambda$	$(2048)^2 \times 1024$	—
Id	0.09	0.09	0.53	40	400	2.13	$(30\lambda)^2 \times 30\lambda$	$(1024)^2 \times 1024$	—
Id	0.09	0.09	0.53	40	800	1.93	$(36\lambda)^2 \times 18\lambda$	$(2048)^2 \times 1024$	—
IIa	0.031	0.09	0.53	20	800	1.10	$(18\lambda)^2 \times 18\lambda$	$(1024)^2 \times 1024$	—
IIb	0.031	0.09	0.53	10	800	1.06	$(18\lambda)^2 \times 18\lambda$	$(1024)^2 \times 1024$	—
IIIa	0.0155	0.045	0.53	40	800	1.09	$(18\lambda)^2 \times 18\lambda$	$(1024)^2 \times 1024$	—
IIIb	0.04	0.12	0.53	40	800	1.22	$(18\lambda)^2 \times 18\lambda$	$(1024)^2 \times 1024$	—
IIIc	0.031	0.2	0.53	40	400	1.15	$(30\lambda)^2 \times 30\lambda$	$(1024)^2 \times 1024$	—
IIIc	0.031	0.2	0.53	40	800	1.12	$(18\lambda)^2 \times 18\lambda$	$(1024)^2 \times 1024$	—
IIId	−0.031	0.24	0.53	40	400	0.86	$(30\lambda)^2 \times 30\lambda$	$(1024)^2 \times 1024$	—
IIId	−0.031	0.24	0.53	40	800	0.89	$(18\lambda)^2 \times 18\lambda$	$(1024)^2 \times 1024$	—
IIIe	−0.11	0.2	0.71	28.5	800	0.80	$(18\lambda)^2 \times 18\lambda$	$(1024)^2 \times 1024$	VERDI

last time step, which is approximately twice the integral length scale ($\sim 2z^*_{\mathrm{end}}$). When using the dimensionalization consistent with the DYCOMS-II radiative-cooling parameters ($\lambda = 15$ m, $F_0 = 70\,\mathrm{W\,m^{-2}}$), the simulations with $\mathrm{Re}_0 = 800$ and $\mathrm{Re}_0 = 1600$ take ~10 min to reach a mixing layer of depth $2z^*_{\mathrm{end}} \simeq 220$ m, the simulations with $\mathrm{Re}_0 = 400$ take ~15 min to reach $2z^*_{\mathrm{end}} \simeq 375$ m, and the simulation with $\mathrm{Re}_0 = 200$ takes ~20 min to reach $2z^*_{\mathrm{end}} \simeq 700$ m. In this last simulation the integral velocity scale reaches $w^* = 0.77\,\mathrm{m\,s^{-1}}$ at the last time step, which is comparable to stratocumulus measurements.

c. Numerics

The numerical algorithm is based on high-order, spectral-like compact finite differences (Lele 1992) and a low-storage fourth-order Runge–Kutta scheme (Carpenter and Kennedy 1994). The time step is set by a Courant condition. All simulations run for ~3500 time steps except for $\mathrm{Re}_0 = 1600$, which runs for 7200 time steps. The pressure Poisson equation is solved using a Fourier decomposition along the periodic horizontal planes x_1Ox_2 and a factorization of the resulting set of equations along the vertical coordinate (Mellado and Ansorge 2012).

All the simulations discussed on this paper have a resolution parameter $\Delta x/\eta$ on the order of 2.0 or less, where Δx is the grid spacing and η is the Kolmogorov length. Using grid convergence studies (not shown), such a resolution has been proved to be enough for accuracies on the order of 2% or better in the statistics discussed in this paper, using the numerical algorithm described above. Further details can be found in Mellado (2010).

4. The buoyancy source

The strength of the evaporative and radiative cooling can be evaluated by their associated integrated buoyancy sources. The radiative-cooling integrated buoyancy source is determined by the temperature of the cloud and by the temperature and composition of the atmosphere, and it is usually approximately well known (Bretherton et al. 1999). On the other hand, the evaporative-cooling integrated buoyancy source is determined by the entrainment dynamics, which are unknown a priori. This means that the relative strength of the two main driving forces in stratocumulus models critically depends on properly resolving the entrainment region, thus producing a large uncertainty in numerical models. We investigate in this section whether the total buoyancy source is well captured in our simulations.

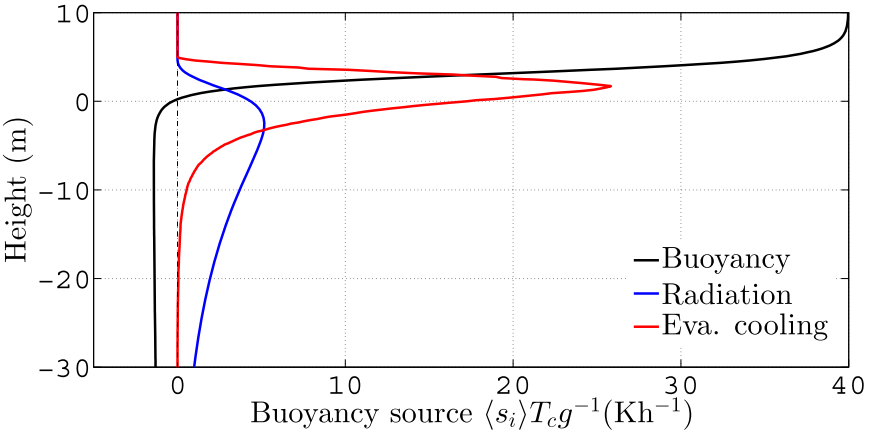

FIG. 1. Horizontally averaged buoyancy sources due to evaporative and radiative cooling for the DYCOMS-II simulation with $\mathrm{Re}_0 = 1600$. The profiles correspond to a CBL depth $2z^* = 235$ m. We have assumed $\lambda = 15$ m for the figures shown in this paper, but all the plots can be rescaled for a different value of λ. The buoyancy profile has been added as a reference. Notice how the evaporative cooling reaches higher values but concentrates on a smaller region close to the inversion.

a. *Computation of the buoyancy source*

To evaluate the buoyancy sources, a diagnostic exact equation for the buoyancy is derived from Eqs. (3) and (5):

$$\begin{aligned} db/dt &= \kappa_T \nabla^2 b - s_{\mathrm{rad}} - s_{\mathrm{eva}}, \\ s_{\mathrm{rad}} &= g(c_p^c T_c)^{-1} \beta r, \quad \text{and} \\ s_{\mathrm{eva}} &= \kappa_T \Delta b \left(\frac{D + \chi_s}{1 - \chi_s}\right) \left(\frac{d^2 f}{d\xi^2}\right) |\nabla \xi|^2, \end{aligned} \tag{8}$$

where s_{rad} and s_{eva} are the buoyancy sources due to radiative and evaporative cooling, respectively. The radiative-cooling source has the same form as the one investigated in De Lozar and Mellado (2013), where radiative cooling was the only process retained in the analysis. The evaporative-cooling source is nonzero only at the interface between saturated and unsaturated air, consistent with the mixing behavior explained in section 2c. This behavior is given by the term $d^2 f/d\xi^2$, which is a function of integral one and width ϵ across the cloud–dry air interface ($\xi = 0$), and tends to a Dirac delta function in the limit $\epsilon \to 0$.

In Fig. 1, we compare the horizontally averaged profiles of the buoyancy sources in our reference case, which corresponds to the reference flight RF-01 from the DYCOMS-II campaign. Both cooling sources are concentrated in a thin region close to the inversion. The radiative source s_{rad} peaks close to the cloud top at $5\,\mathrm{K\,h^{-1}}$ and decays exponentially over a length scale $\lambda = 15$ m. When comparing with literature results, the radiative cooling is often given in terms of $r/c_p \propto \beta^{-1} s_{\mathrm{rad}}$. This function peaks at $10\,\mathrm{K\,h^{-1}}$, in agreement with the calculations of Larson et al. (2007) for the same flight. The maximum evaporative cooling s_{eva} is 5 times higher ($25\,\mathrm{K\,h^{-1}}$) than the maximum radiative cooling, but it also concentrates on a thinner region close to the cloud top.

The driving strength of radiative and evaporative cooling can be given by their respective integrated buoyancy sources:

$$\begin{aligned} S_{\mathrm{rad}} &= \int \langle s_{\mathrm{rad}} \rangle \, dz = \beta B_0 \quad \text{and} \\ S_{\mathrm{eva}} &= \int \langle s_{\mathrm{eva}} \rangle \, dz, \end{aligned} \tag{9}$$

where the angle brackets symbolize the horizontal average. This measure can be considered as a generalization of previous studies, in which the strength of both mechanisms is directly evaluated from the linearized buoyancy function in Eq. (5) (e.g., Yamaguchi and Randall 2012).

Equation (9) shows that the integrated buoyancy source due to radiative cooling, S_{rad}, is constant in time in a cloud-top mixing-layer configuration. The same is true for stratocumulus under the condition that they are optically thick (i.e., that the cloud depth is much larger than the extinction length λ). When introducing latent heat effects, the radiative buoyancy source decreases because a fraction $(1 - \beta)$ of the radiative cooling is used for the condensation of cloud droplets. In the limit of no evaporation ($\beta = 1$), $S_{\mathrm{rad}} = B_0$ is the total source of buoyancy as in the smoke cloud (Bretherton et al. 1999). In general, $\beta \simeq 0.5$, so that only half of the radiative

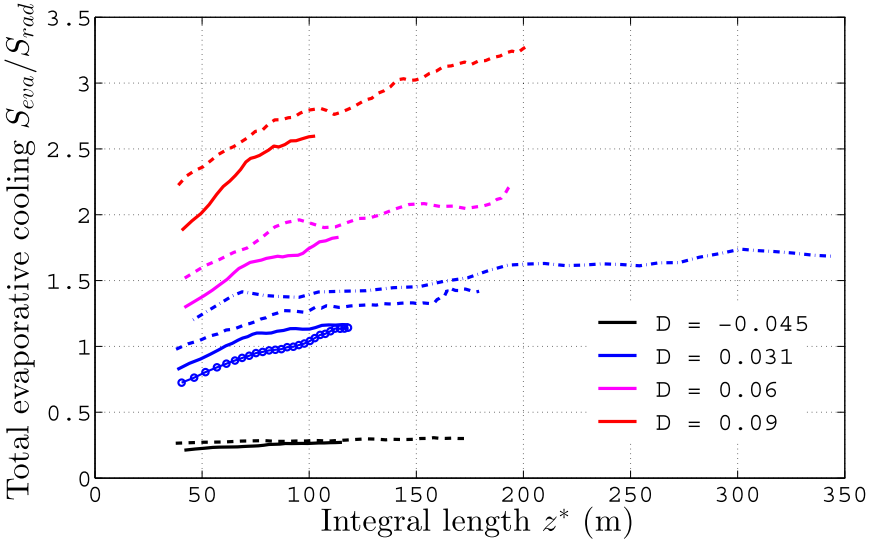

FIG. 2. Ratio of the integrated buoyancy sources: evaporative cooling over the radiative cooling. The ratio is plotted as a function of the integral scale for the simulations of the first group. The colors denote D, and the line types show values of Re_0: 1600 (circles), 800 (solid), 400 (dashed), and 200 (dotted–dashed).

cooling acts directly on the buoyancy, as already noted by some authors (e.g., van Zanten and Duynkerke 2002). Since S_{rad} quantifies the direct impact of radiation on the buoyancy, we have found it more natural to use S_{rad} instead of B_0 to scale many of the results presented in this paper.

Figure 2 shows the evolution of the integrated buoyancy source due to evaporative cooling S_{eva} as a function of z^* for the simulations of the group I in which we vary the BRI parameter D. Only the simulations of group I are shown, because these are the ones with better statistical convergence. We observe that evaporative cooling increases with viscosity when keeping all other parameters constant (lines with same color but different style). The differences are especially large for the BRI cases ($D > 0$), in which S_{eva} increases by ~10% when the viscosity is doubled. This viscosity dependence is in line with previous stratocumulus LES, where entrainment, and so S_{eva}, are considerably enhanced by diffusion (e.g., Stevens et al. 2005). It is usually argued that this problem arises because of the limited resolution employed in LES, but we observe that the viscosity dependence does not disappear even when the Kolmogorov scale of the resolved flow is below 10 cm.

b. The BRI correction

Mellado (2010) investigated the BRI in a cloud-top mixing layer driven solely by evaporative cooling. He found that the inversion thickness is determined by a balance of diffusion and the negative buoyancy generated by the BRI. This balance sets a constant diffusive flux into the cloud that governs the entrainment. The resulting inversion thickness h_{diff}, entrainment velocity w_e^{diff}, and integrated buoyancy source S_{diff} are

$$h_{\mathrm{diff}}(\nu) = \frac{10}{f_1(\chi_s + D)^{2/3}}\left[\frac{\nu^2(1+D)^2}{D\Delta b}\right]^{1/3},$$
$$w_e^{\mathrm{diff}} = \nu/h_{\mathrm{diff}}, \quad \text{and}$$
$$S_{\mathrm{diff}} = (1 + D/\chi_s)w_e^{\mathrm{diff}}\Delta b, \tag{10}$$

where $f_1 \simeq 1.3$ is a numerical constant, whose value was obtained from the simulations. The quantities defined by Eq. (10) explicitly depend on viscosity and are called "diffusive" in this paper (note that in our DNS they are independent of the numerics). For the viscosity of air, the diffusive entrainment velocity and buoyancy source are negligible ($w_e^{\mathrm{diff}} = 0.15\,\mathrm{mm\,s^{-1}}$ and $S_{\mathrm{diff}} \simeq 1\,\mathrm{W\,m^{-2}}$) when compared to measurements ($w_e \simeq 2$–$5\,\mathrm{mm\,s^{-1}}$), indicating that evaporative cooling alone cannot control the stratocumulus-top dynamics. When using an enhanced viscosity, the corresponding diffusive source increases by a factor $(\nu/\nu_{\mathrm{air}})^{1/3}$. This scaling can also be obtained from dimensional analysis, when considering the balance between diffusion and the buoyancy perturbation introduced by the BRI b_s. For our reference case with the lowest viscosity the diffusive cooling is $S_{\mathrm{diff}} \simeq 8\,\mathrm{W\,m^{-2}}$, approximately 20% of S_{eva} and therefore nonnegligible.

Our hypothesis is that this diffusive balance also sets the local inversion thickness in the simulations with BRI even if other forcing mechanisms are present, provided

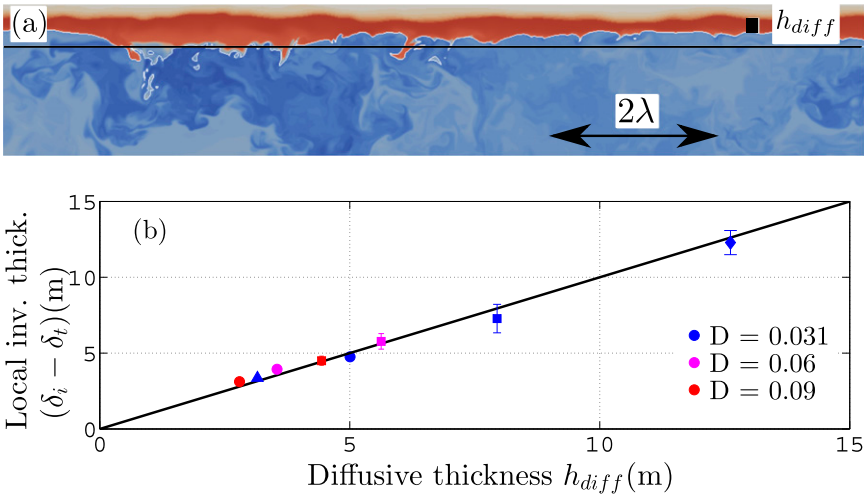

FIG. 3. (a) Buoyancy at the inversion for the DYCOMS-II case ($Re_0 = 1600$). The color scale has been chosen to highlight the local inversion thickness together with the flow structures. The blue scale covers the range $-0.08 < b/\Delta b < 0$; the red scale covers $0 < b/\Delta b < 0.95$. The black box represents the diffusive thickness h_{diff}, and the arrow indicates the radiation extinction length λ. The black line marks the height of the inversion point, and the white contour is the cloud boundary as given by the isosurface $q_l = 10^{-3} q_l^c$. The snapshot represents a region 155 m wide. (b) Local inversion thickness as a function of the diffusive inversion thickness [see Eqs. (10) and (11)]. Each point corresponds to the local thickness averaged during the second half of the simulations. The error bar represents 3 times the standard deviation. The colors represent D, and the symbols give values of Re_0: 1600 (triangles), 800 (circles), 400 (squares), and 200 (diamonds).

that the stratification is strong enough for the cloud interface to remain relatively flat. The underlying assumption is that the aforementioned balance at the cloud interface decouples from the radiative forcing and the turbulence in the cloud. To test this hypothesis we present in Fig. 3a a snapshot of the cloud top in which the inversion layer is highlighted by the red scale. Notice that the local thickness of the inversion layer is well represented by the diffusive inversion thickness h_{diff} given by Eq. (10), supporting our hypothesis.

A more quantitative comparison is obtained from estimating the local thickness of the inversion δ_l from the averaged inversion thickness δ_i. We define the averaged inversion thickness as the distance in which the horizontally averaged buoyancy profile varies from its cloud value ($b^c = 0$) to 95% of the buoyancy jump Δb. The averaged thickness δ_i differs from the local thickness δ_l because the averaged one includes a small deformation of the inversion by the large turbulent eddies δ_t:

$$\delta_i = \delta_l + \delta_t, \tag{11}$$

where δ_t can be inferred from a simple balance of potential and kinetic energy (see, e.g., Haman 2009):

$$\delta_t = C(w^*)^2/\Delta b, \tag{12}$$

with w^* being the integral velocity defined in Eq. (16) and C a constant of order unity. Figure 3b shows the local inversion thickness δ_l [Eq. (11)] as a function of the diffusive scale h_{diff} for all the BRI simulations. We use $C = 2$ because this value minimizes the temporal variations in δ_l. In general, h_{diff} provides a very good approximation for the local thickness, confirming the visual impression in Fig. 3a.

c. *The inviscid contribution*

In Fig. 4 we present the integrated evaporative-cooling buoyancy source, once the diffusive contribution S_{diff} [Eq. (10)] is subtracted. All curves with the same D but different viscosities collapse. This Re_0 independence indicates that the diffusive flux is captured by the diffusive instability and that most of the small-scale turbulent mixing occurs at the resolved scales. As a result, we identify $S_{eva} - S_{diff}$ as the inviscid contribution to the integrated buoyancy source due to evaporative cooling.

The inviscid integrated buoyancy source due to evaporative cooling increases with z^* in Fig. 4. This increase is related to the direct cooling contribution to the entrainment as explained in section 6. The rate of growth of the direct cooling with z^* decreases with increasing z^*, with the consequence that the evaporative

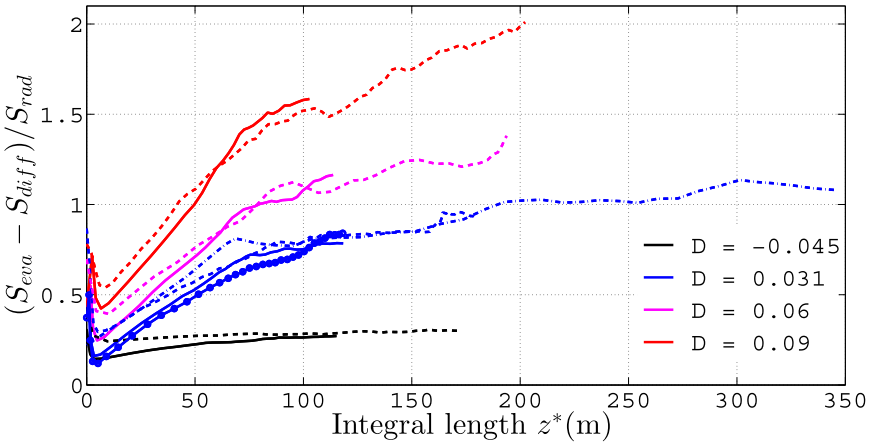

FIG. 4. Ratio of the integrated buoyancy sources: inviscid evaporative cooling over the radiative cooling. The inviscid evaporative cooling has been calculated by removing the diffusive contribution S_{diff} given by Eq. (10), from the total evaporative cooling. The ratio is plotted as a function of the integral scale. The colors denote D, and the line types represent values of Re_0: 1600 (circles), 800 (solid), 400 (dashed), and 200 (dotted–dashed).

cooling seems to saturate for $z^* \gtrsim 250\,\text{m}$. The Re_0 independency together with the z^* saturation confirms that all scales relevant for turbulent mixing are resolved in our simulations. This gives us confidence to extrapolate the results of our DNS to atmospheric conditions once the diffusive contribution is removed.

5. The inversion point

The inversion point was originally introduced by Lilly (1968) in order to describe the exchange of energy and water between the cloud and the free atmosphere in a zero-order mixed-layer model. In such a simplified model the flux of water and energy at the inversion point directly quantifies the aforementioned exchange. The extension of this concept to more realistic representations of the vertical structure of the inversion is however nontrivial owing to the existence of a finite-thickness layer, called the entrainment interfacial layer or entrainment zone, between the cloud and the free atmosphere. A natural extension of the inversion point concept is to redefine the inversion point as the interface between the entrainment zone and the cloud layer and then to investigate the exchange of water and energy at this point. Two problems arise when extending the definition of the inversion point. First, the energy balance becomes more complex than in the zero-order model owing to new terms that account for the cooling and deformation of the entrainment zone. Second, the entrainment zone is not uniquely defined, and therefore the choice of the inversion point is not unique.

Any definition of the inversion point z_i serves to divide the rate of change of total buoyancy into two contributions:

$$\frac{d}{dt}\int_{-\infty}^{z_i} \langle b\rangle\, dz = -Q_{\text{cbl}} \quad \text{and}$$
$$\frac{d}{dt}\int_{z_i}^{\infty} \langle b\rangle\, dz = -Q_{\text{inv}}, \tag{13}$$

where Q_{cbl} represents the in-cloud cooling and Q_{inv} represents the entrainment-zone cooling. The in-cloud region and entrainment zone are specified by the inversion point definition. The entrainment-zone cooling Q_{inv} can be written as

$$Q_{\text{inv}} = \frac{dz_i}{dt}\Delta b + \frac{d}{dt}\left[\int_{z_i}^{\infty} (\Delta b - \langle b\rangle)\, dz\right], \tag{14}$$

where the first term of the right-hand side accounts for the inversion point motion, where

$$w_e = dz_i/dt \tag{15}$$

is the entrainment velocity, and the second term is a shape term that quantifies the deformation of the cloud interface.

The challenge is to choose an inversion point that yields a balance of buoyancy, as given by Eq. (13), that is useful to understand the cloud dynamics. Following our previous work in a cloud-top mixing layer driven solely by radiative cooling (De Lozar and Mellado 2013) we choose the inversion point as the height of neutral

buoyancy $\langle b\rangle(z_i) = 0$. In this section we validate this choice by presenting scalings that show that, first, the corresponding in-cloud cooling $Q_{\rm cbl}$ characterizes the convective movements in the cloud, and second, that the corresponding entrainment-zone cooling $Q_{\rm inv}$ relates to the evaporative cooling caused by the entrainment.

a. Scaling of the integral quantities inside the cloud

This scaling is based on the observation that the flow in a cloud-top mixing layer resembles an inverse convective boundary layer (CBL) that is driven from the top. If the flow inside the cloud behaves as in a CBL, the buoyancy flux driving the convective flow should then be related to the in-cloud cooling $Q_{\rm cbl}$, assuming that the inversion point is well defined. In De Lozar and Mellado (2013) we showed that integral properties of the flow in the in-cloud region follow typical convective scalings when redefining the reference buoyancy flux $B_{\rm ref}$ such that

$$
\begin{aligned}
B_{\rm ref} &= \left[\int_{t_0}^{t} Q_{\rm cbl}(t')\,dt'\right](t-t_0)^{-1},\\
z^* &= \frac{1}{B_{\rm ref}}\int \langle w'b'\rangle\,dz,\\
w^* &= (B_{\rm ref}z^*)^{1/3}, \quad \text{and}\\
b^* &= B_{\rm ref}/w^*,
\end{aligned}
\tag{16}
$$

where z^*, w^*, and b^* are the integral length, velocity, and buoyancy scale as defined by Deardorff (1970), and t_0 is the initial time of the simulations. The integration time $t - t_0$ is an estimation for the time that takes for the CBL to adapt to variations in the buoyancy flux $Q_{\rm cbl}$, and it is approximately twice as long as the large-eddy turnover time $t^* = z^*/w^*$. The only difference with the radiative-cooling-only scaling is that the in-cloud cooling $Q_{\rm cbl}$ now includes a nonnegligible contribution due to the evaporation of droplets in the in-cloud region.

In the fully developed turbulent regime, averaged flow properties scale with the convective scales so that they are independent of time and just depend on the self-similar variable $\xi = (z - z_i)/z^*$ (Mellado 2012). Figure 5 shows the scaled velocity fluctuations and mean buoyancy as a function of the self-similar variable ξ for all our simulations. Each curve represents the average over several time steps starting from $z^*/\lambda = 6$, which is our estimate for the beginning of the fully developed regime where initial conditions are sufficiently forgotten. Together with our simulations, the results of a cloud-top mixing layer driven solely by evaporative cooling (Mellado 2010) are also shown in green, where the shadowed region represents typical variations due to lack of statistical convergence. All our results show an excellent collapse indicating that $B_{\rm ref}$ is indeed the relevant buoyancy flux driving the flow in the cloud, thus justifying our election of the inversion point. Moreover, since this convective scaling is an inviscid scaling, the collapse proves that the flow has started to reach the Reynolds number–independent regime (as given by Re*) in the in-cloud region.

b. Entrainment scaling

Using the level of vorticity fluctuations, we can differentiate between a region with irrotational flow, which comprises the free atmosphere and part of the inversion layer, and a region where the flow is rotational, and hence turbulent, which comprises the in-cloud region and the turbulent part of the inversion layer. Consistently with the dynamics of a turbulent–nonturbulent interface, irrotational flow is regularly entrained into the turbulent region, whereas the turbulent flow cannot mix into the irrotational region. These entrainment events provide the dry air necessary for the evaporation of droplets at the stratocumulus top, even when the details of how and where the evaporation actually happens might be complex. In this section we use this observation in order to find a relationship between the total evaporative-cooling buoyancy source $S_{\rm eva}$ with the entrainment of dry air into the cloud, as quantified by $Q_{\rm inv}$.

We assume quasi-steady mixing dynamics at the cloud top. Quasi-steady dynamics are defined by the condition that the volume fraction and composition of unsaturated air in the turbulent region of the flow (i.e., the unsaturated air between the free atmosphere and the cloudy air) varies slowly when compared with the entrainment dynamics. In other words, the volume fraction and composition of unsaturated air in the inversion layer and in cloud holes is approximately constant. Here we refer to cloudy air as the condensate-laden air, which is different to the in-cloud region previously defined. Quasi-steady mixing dynamics can be expected when the separation of scales between the entrainment dynamics, characterized by λ, and the convective dynamics, characterized by z^*, is large enough.

The total evaporative-cooling buoyancy source is calculated by taking the time derivative of the horizontally averaged volume-integrated buoyancy [Eq. (5)] in the case of no radiation ($r = \psi = 0$):

$$
S_{\rm eva} = -\frac{\Delta b}{q_l^c}\frac{D+\chi_s}{1-\chi_s}\frac{d}{dt}\left(\int \langle q_l\rangle\,dz\right)_{\rm eva},
\tag{17}
$$

where the domain of the integral is the cloud and the entrainment region (in our simulations it is the whole domain). The derivative accounts only for changes in liquid due to evaporation.

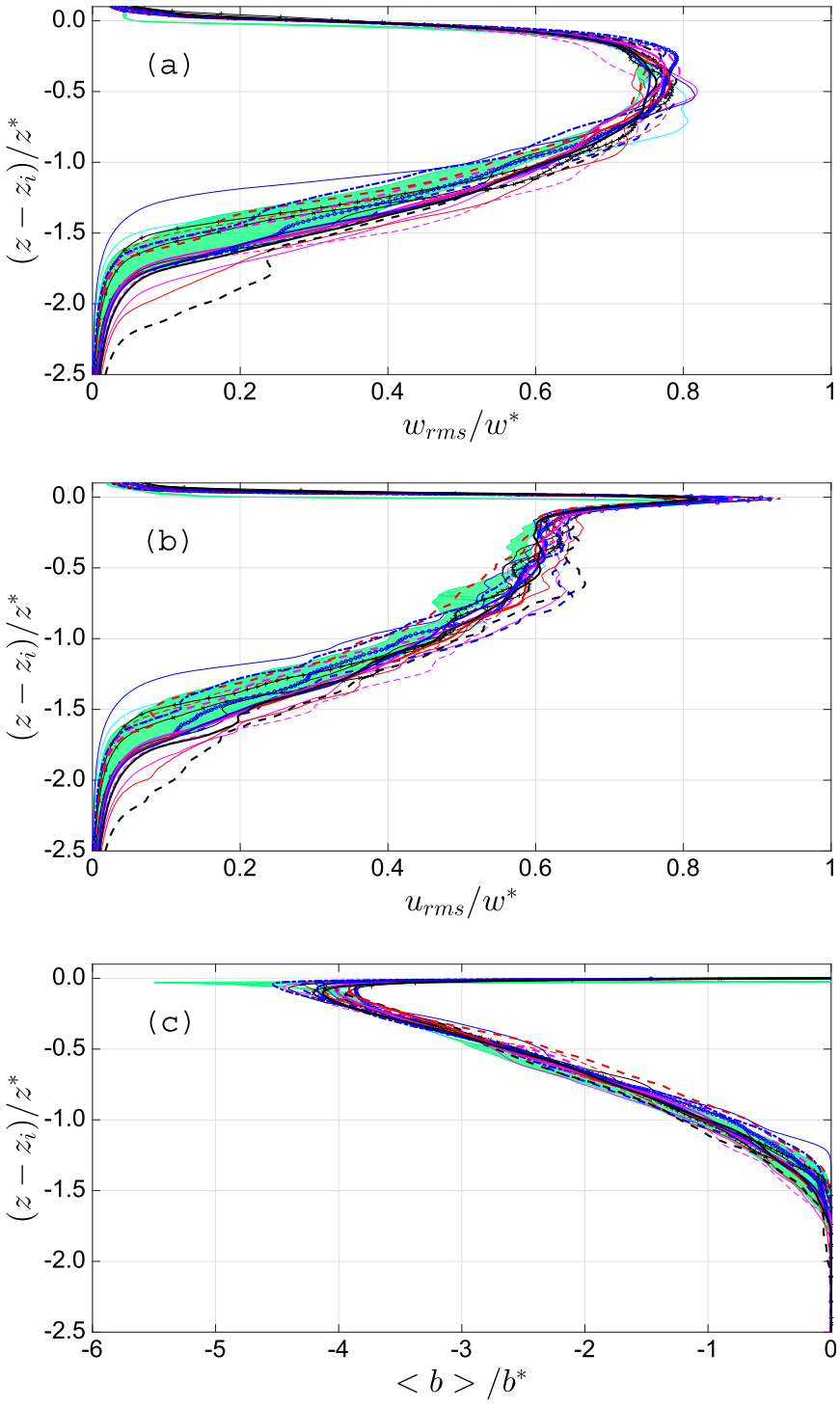

FIG. 5. Self-similar vertical profiles of (a) vertical velocity fluctuations $w_{\mathrm{rms}} = \sqrt{\langle w'w' \rangle}$, (b) horizontal velocity fluctuations $u_{\mathrm{rms}} = \sqrt{\langle u'u' \rangle + \langle v'v' \rangle}$, and (c) mean buoyancy. The profiles are averaged from $z^* \sim 6\lambda$ once the flow reaches the fully developed regime. The thicker lines correspond to the experiments of the first group and are described in the caption of Fig. 2. The black crosses correspond to the modified stratification experiments of the second group (where $\times$ represents IIa with $\mathrm{Ri}_0 = 20$, and $+$ represents IIb with $\mathrm{Ri}_0 = 10$). The thinner lines correspond to the experiments of the third group: IIIa (black), IIIb (blue), IIIc (magenta), IIId (red), and the VERDI case (cyan). The line types denote Re_0: 800 (solid) and 400 (dashed). The shadowed green area shows the result of a cloud-top mixing layer driven solely by evaporative cooling from Mellado (2010).

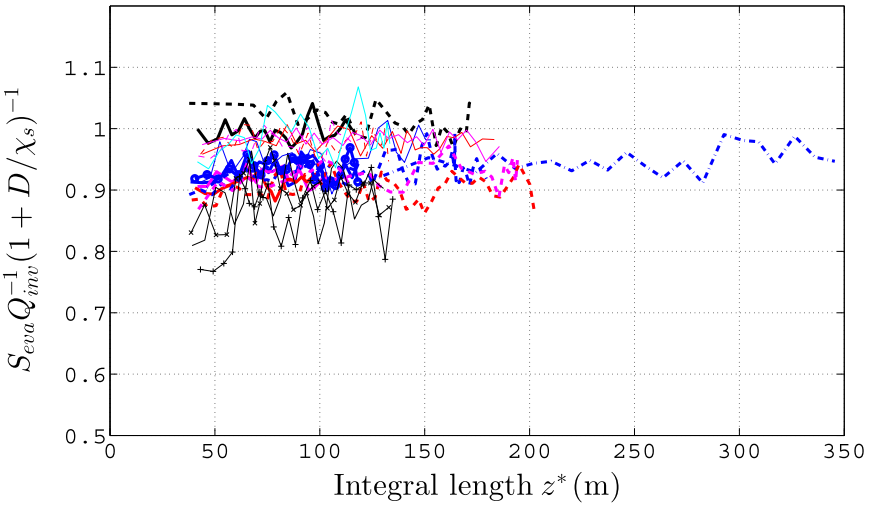

FIG. 6. Scaling relating the inversion cooling Q_{inv} with the total evaporative cooling S_{eva} as given by Eq. (20). The legend is explained in Fig. 5.

To evaluate the changes in liquid water due to evaporation, let us consider an entrained parcel from the free atmosphere with volume dv_d. After the entrainment event the dry-air parcel mixes within the turbulent region, both with unsaturated and cloudy air. When assuming quasi-steady dynamics, the volume of entrained dry air, which is mixed into the unsaturated air, has to be compensated by an equivalent volume of dry air mixing out the unsaturated air, because the composition and volume fraction of the unsaturated air cannot change. Since no air can return to the free atmosphere, this volume of dry air has to mix with cloudy air. As a result, the entrainment event causes that a volume of dry air dv_d (not necessarily the same air) is mixed (directly or indirectly) with cloudy air.

Let us consider the mixing process of dry with cloudy air as a sequence of two stages. In a first stage, the mixing process continues until the volume of dry air dv_d is at saturation ($\chi = \chi_s$). From the definition of χ_s in the linear formulation, the volume of cloudy air needed to bring this volume of dry air to saturation is given by

$$dv_c = \frac{1-\chi_s}{\chi_s} dv_d. \tag{18}$$

The just-saturated air does not contain any liquid water, which means that all liquid initially contained by dv_c has evaporated. If q_l^c is the liquid specific humidity in the cloud, the mass of liquid that evaporates is quantified by $\rho_0 q_l^c dv_c$. In a second stage, any further mixing of the saturated air with cloudy air does not produce any extra evaporation because the mixing process always involves fully saturated air (see section 2). Therefore, we can conclude that $\rho_0 q_l^c dv_c$ is the induced evaporated water when a parcel of dry air of volume dv_d is entrained into the cloud.

Integrating Eq. (18) for all entrained parcels and taking the time derivative, we obtain

$$\frac{d}{dt}\left(\int \langle q_l \rangle \, dz\right)_{\text{eva}} = -\frac{1-\chi_s}{\chi_s}\frac{q_l^c}{A}\frac{d}{dt}\left(\int dV\right)_{\text{ent}}, \tag{19}$$

where the last term refers to the rate of entrained dry air into the cloud and A is the area of the integrated volume used in the surface averages.

The last step consists in estimating the rate of entrainment of dry air $d(\int dV)_{\text{ent}}/dt$. In De Lozar and Mellado (2013), we showed that the rate of entrainment of dry air (and of any conserved scalar) is well approximated by $(Q_{\text{inv}}\Delta\chi A)/\Delta b$, where $\Delta\chi = 1$ when the scalar is the mixing fraction. This condition is necessary for the synchronized motion of the buoyancy and dry air. Combining Eqs. (17) and (19) and the approximation for the entrainment rate of dry air, we reach a simple expression that relates the entrainment-zone cooling with the total evaporative cooling (in both the entrainment zone and the in-cloud region):

$$S_{\text{eva}} = Q_{\text{inv}}(1 + D/\chi_s). \tag{20}$$

Figure 6 shows that the balance given by Eq. (20) is approached asymptotically in all our simulations, supporting the validity of our assumptions. The deviations at the early stages are mainly due to the time needed to reach quasi-steady dynamics.

In the case of negligible deformation of the inversion, the above-described approximation for the entrainment of dry air reduces to the entrainment condition of the

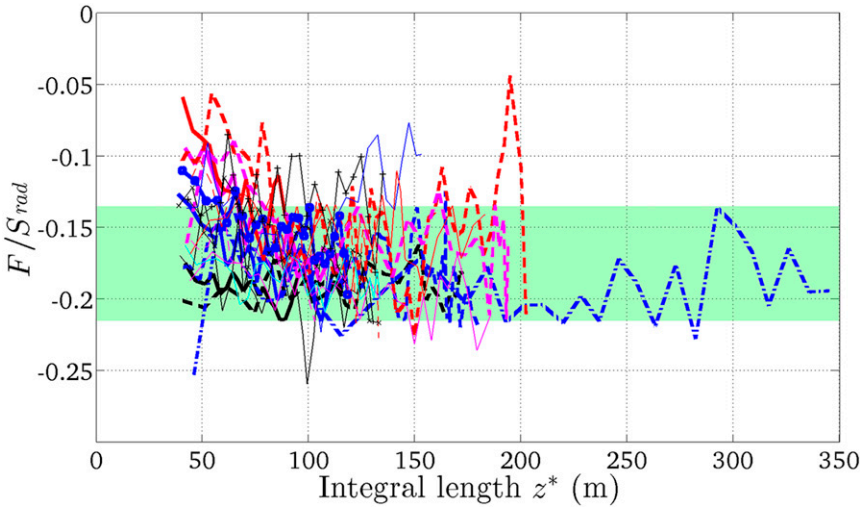

FIG. 7. Buoyancy flux at the inversion point. This flux quantifies the buoyancy exchange between the cloud and the entrainment zone. The shadowed area highlights the region $F = (0.175 \pm 0.04)S_{\text{rad}}$. The legend is explained in Fig. 5.

zero-order model ($d(\int dV)_{\text{ent}}/dt = w_e A$). This allows us to rewrite Eq. (19) in a form that provides an approximated relation between the total evaporated water and the entrained velocity:

$$-\frac{d}{dt}\left(\int \langle q_l \rangle \, dz\right)_{\text{eva}} = \frac{1-\chi_s}{\chi_s} w_e q_l^c , \tag{21}$$

which can be directly used to relate the total evaporative cooling of the cloud to the entrainment velocity by multiplication by the latent heat. Equation (21) also recovers the ratio between the entrainment velocity and cloud cooling for the evaporative-cooling-only case S_{diff} in Eq. (10).

Equation (20) serves as a validation for the choice of the inversion point because it relates a property that critically depends on the definition of z_i, Q_{inv}, with an integral quantity S_{eva} which is independent of z_i. The excellent agreement of Eq. (20) with our simulations further validates our choice for the inversion point and gives us confidence for the results that follow from this choice. These results are presented in the next section.

6. The inversion cooling

We quantify the mechanisms that contribute to the entrainment-zone cooling by integrating Eq. (8) with our definition for the inversion point:

$$-Q_{\text{inv}} = \underbrace{\langle w'b' \rangle_{z_i}}_{F_{\text{turb}}} \underbrace{-\kappa_T \left\langle \frac{\partial b}{\partial z} \right\rangle_{z_i}}_{F_{\text{mol}}} \underbrace{-\int_{z_i}^{\infty} \langle s_{\text{rad}} \rangle \, dz}_{S_{\text{rad}}^{\text{inv}}} \underbrace{-\int_{z_i}^{\infty} \langle s_{\text{eva}} \rangle \, dz}_{S_{\text{eva}}^{\text{inv}}} , \tag{22}$$

where the turbulent flux F_{turb} and the molecular flux F_{mol} quantify the exchange of buoyancy between the entrainment zone and in-cloud layer. The two source terms, $S_{\text{rad}}^{\text{inv}}$ and $S_{\text{eva}}^{\text{inv}}$, quantify the decrease of buoyancy at the entrainment zone due to radiative and evaporative cooling, respectively. The radiative source $S_{\text{rad}}^{\text{inv}}$ is known as direct cooling in the literature (see, e.g., Wood 2012). The name "direct" comes in contraposition to the radiative cooling of the in-cloud region, which contributes only indirectly to the entrainment through the buoyancy fluxes F in Eq. (22) by intensifying the in-cloud turbulence. Analogous to the radiative cooling, only part of the evaporative cooling, defined as direct evaporative cooling $S_{\text{eva}}^{\text{inv}}$, occurs in the entrainment zone.

a. *The flux between the entrainment zone and the cloud*

The flux of buoyancy between the entrainment zone and the in-cloud region has a turbulent and a molecular component: $F = F_{\text{turb}} + F_{\text{mol}}$. Despite the high resolution we employ in our calculations, the molecular flux is nonnegligible. In the DYCOMS-II simulations the molecular flux contribution ranges from 40% to 12% of the total flux, when increasing the Reynolds number from $\text{Re}_0 = 200$ to $\text{Re}_0 = 1600$. For the other simulations the relative contribution of the molecular flux generally increases with the buoyancy reversal parameter D, reaching values comparable to the turbulent flux (up to 45% of the total flux) for the combinations of high D and low Re_0.

Although the molecular contribution can be relatively large, we do not see any dependence of the total flux F on Re_0. In Fig. 7, the results of all the simulations

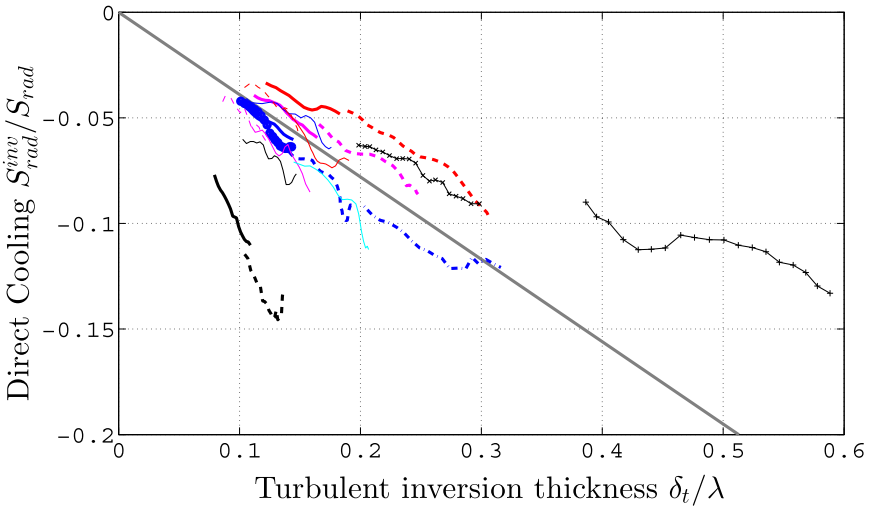

FIG. 8. Direct cooling due to radiation as a function of the ratio of the turbulent inversion thickness over the extinction length. The gray line represents $S^{\text{inv}}_{\text{rad}} = 0.39(\delta_t/\lambda)S_{\text{rad}}$, as motivated by the smoke-cloud simulations in De Lozar and Mellado (2013). The legend is explained in Fig. 5.

collapse to $F = (0.175 \pm 0.04)S_{\text{rad}}$, where the error interval is given by the statistical convergence of our simulations. This result is identical to that obtained in the radiative-only case in De Lozar and Mellado (2013). The only simulation that seems to depart from the statistically significant region has the lowest Reynolds number ($\text{Re}_0 = 200$), suggesting that low–Reynolds number effects can appear for $\text{Re}_0 \leq 200$. The collapse of the other simulations confirms that all flow scales that are relevant for the inviscid exchange between the cloud and the entrainment zone are well resolved.

After an initial transient ($z^* > 4\lambda$) the total flux F in Fig. 7 seems insensitive to the size of the largest scales in the flow z^*. This is in agreement with our proposition in De Lozar and Mellado (2013) that only eddies smaller than 4λ (or 60 m) are relevant for the turbulent entrainment process and supports the use of a cloud-top mixing layer to study some aspects of the entrainment process in the STBL.

b. *The radiative direct cooling*

In the case of the smoke cloud, De Lozar and Mellado (2013) showed that the direct cooling, $S^{\text{inv}}_{\text{rad}}$, is a function of the ratio of the averaged inversion thickness δ_i (defined in section 4b) over the extinction length λ. This scaling is based on the assumption that the smoke is a conserved scalar and spreads over the whole entrainment zone. This assumption, however, does not apply for liquid clouds. The liquid field spreads locally only over a small fraction of the entrainment zone, because droplets evaporate completely when the mixing fraction reaches χ_s.

To estimate the direct cooling in liquid clouds we have to consider only the fraction of the inversion thickness that is occupied by liquid. This is estimated by looking at the decomposition of the inversion-layer thickness into a local and a turbulent component given in Eq. (11). As a first approximation, we assume that the liquid occupies a fraction infinitely thin of the local inversion thickness δ_l, which is consistent with the typically small values of χ_s in stratocumulus. This assumption is also consistent with Fig. 3a, where the liquid (white contour) rarely enters the local inversion (in red). According to this hypothesis, the fraction of the averaged inversion thickness occupied by the liquid field is determined only by the undulations of the inversion, and this is quantified by the turbulent inversion thickness δ_t defined by Eq. (12). As a consequence, we expect that the scaling for the direct cooling in the smoke and liquid cloud are similar when redefining the inversion thickness as δ_t/λ in the case of the liquid cloud.

Figure 8 shows the direct cooling $S^{\text{inv}}_{\text{rad}}$ as a function of the ratio of turbulent inversion thickness to the extinction length δ_t/λ. The gray line shows the scaling predicted for the only radiative-cooling case (De Lozar and Mellado 2013) for a similar stratification, when changing the definition of the inversion thickness as discussed above. This gray line captures the main tendencies of our results, supporting our assumptions.

The radiation model employed in the radiative-only simulations (De Lozar and Mellado 2013) is different than the one employed in this paper, although both are still one dimensional. The difference is that in this paper we use local values of the liquid water content ℓ for the

calculations of the radiative function r in Eq. (4), while in the radiative-only case we used the plane-average value $\langle \ell \rangle$. The agreement of both experiments shows that our calculations of the direct cooling are independent of the details of the radiation model. This was confirmed by extra simulations of the smoke cloud using the model described in this paper, where the results did not change beyond the statistical convergence.

Only two cases depart from the general trend imposed by the smoke-cloud scaling in Fig. 8. The first case corresponds to a very large radiative forcing, or equivalently a low stratification, and it is represented by the black crosses in the right part of Fig. 8. This means that the magnitude of the direct cooling decreases for the low stratifications—a behavior that we also found in the smoke simulations. We explain this behavior as in De Lozar and Mellado (2013): a low stratification allows for a fast entrainment that causes the dilution of the mixture of liquid and dry air in the entrainment zone. A diluted mixture increases the radiative extinction length over its reference value λ, thus decreasing the direct cooling for a constant inversion thickness. The second departing case corresponds to very low evaporative cooling (DYCOMS-II case but with $D = -0.045$), and it is represented by the black curves on the left of Fig. 8. We explain the high values of direct cooling found here using the same argument as the previous case: low entrainment and rapid radiative condensation of liquid (when compared to the other cases) increase the liquid content close the cloud top, effectively decreasing the extinction length. Consistent with this explanation, we have observed that the liquid water content in this case reaches particularly high values close to the cloud top when compared to the other cases.

Contrary to our results in the smoke cloud, Fig. 8 shows that the direct cooling is to a first approximation independent of the viscosity (as measured by Re_0). This justifies the approximation of a very thin local inversion to estimate the direct cooling because the thickness of the local inversion varies considerably when changing the viscosity. This result implies that the resolution requirements for calculating the direct cooling in stratocumulus are less demanding than in the smoke simulations.

7. Implications for LES and entrainment models

a. *Implications for LES: Enhanced w_e and the κ criterion*

The κ criterion hypothesizes that stratocumulus breakup and the resulting cloud fraction can be roughly predicted by a function of one single parameter $\kappa = \Delta\Theta_e/(L\Delta q_t)$, where Θ_e is the equivalent potential temperature, and L is the latent heat. Curiously, this criterion can be motivated in two opposite limits: when the entrainment velocity diverges for the conditions of the BRI (Randall 1980; Deardorff 1980) or when the entrainment flux is independent of the evaporative-cooling forcing (van der Dussen et al. 2014). Although many LES (Sandu and Stevens 2011; Lock 2009) show a clear correlation between κ and cloud fraction, there is still some discussion regarding the validity of the κ criterion because of the low resolution typically used in LES (e.g., Sandu and Stevens 2011). The analysis of satellite observations of Yue et al. (2013) hints that the κ criterion might be useful, but it also shows important discrepancies with LES: observations consistently show higher cloud fractions and a less clear correlation of κ with cloud fraction. Here, we examine the implications of the diffusive instability discussed in section 4 for the κ criterion, as both are closely related to the BRI.

The cloud-breakup time is related to the time that it takes a cloud to be desiccated only by entrainment (Yamaguchi and Randall 2008). The desiccation time t_{de} is calculated by assuming a well-mixed boundary layer of depth H with a flux $w_e\Delta\chi$ at the cloud top. In this setup, t_{de} is the time it takes for the mean value of χ inside the boundary layer to increase from $\chi = 0$ to $\chi = \chi_s$. When χ_s is small, the desiccation time is well approximated by

$$t_{\mathrm{de}} = (H\chi_s)/w_e. \tag{23}$$

We consider the limit in which the diffusive entrainment given by the BRI [described by Mellado (2010) and discussed in section 4] is the only entrainment mechanism. In this limit, the entrainment velocity is given by Eq. (10). By using Eqs. (10) and (23), we calculate the desiccation time given by diffusion for a wide variety of cloud-top thermodynamic conditions. Figure 9 shows that this desiccation time is roughly a function of κ and a reference time t_0, which is defined as

$$t_0 = 5H(\nu\Delta b_1)^{-1/3}, \tag{24}$$

which only depends on viscosity and on the boundary layer height. The term $\Delta b_1 = 3.58 \times 10^{-2}\,\mathrm{m\,s^{-2}}$ is a reference buoyancy jump for 1-K stratification.

The reference time t_0 provides a measure of the diffusive contribution. Using $H = 800$ m in Eq. (24), we get $t_0 \simeq 125$ h for air viscosity, confirming again that this instability is irrelevant in the atmosphere. For the viscosity in our DNS, $t_0 \simeq 22$ h is longer though still comparable with the time scale of other processes in the cloud. In LES, the determination of t_0 is not obvious because the effective viscosity is usually unknown. Assuming that numerical diffusion is the main contributor

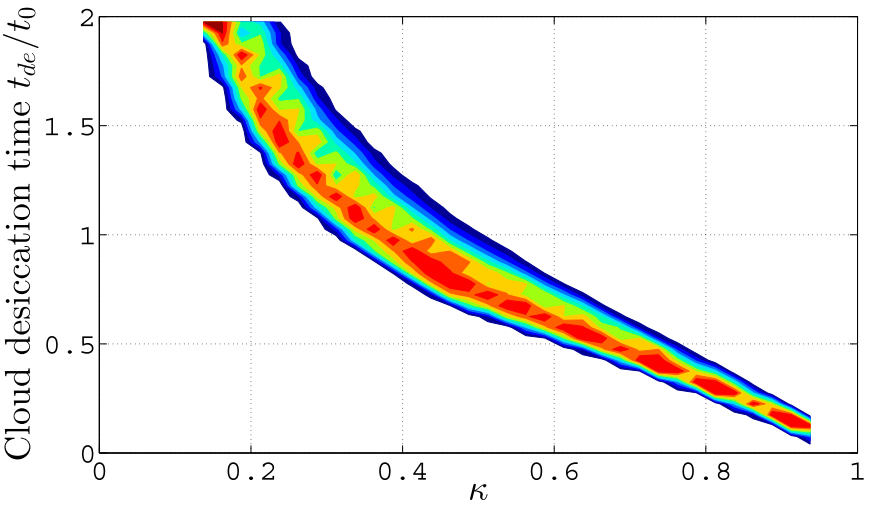

FIG. 9. Diffusive cloud desiccation time as a function of κ, when the BRI parameters are varied in the intervals: $0 < D < 0.3$, $0.03 < \chi_s < 0.4$, and $0.0125 < \Delta b/g < 0.025$. The likelihood of a result is color coded, decreasing from red to blue.

to the viscosity in the inversion, this can be estimated as $\nu_{\text{num}} \sim U\Delta z$ (Patankar 1980), where U is a typical velocity and Δz is the grid spacing. Using $U = 0.1\,\text{m s}^{-1}$ and $\Delta z = 5\,\text{m}$, Eq. (24) gives $t_0 \sim 3\,\text{h}$, comparable to the desiccation times found in LES that are driven solely be evaporative cooling and that use that resolution (Yamaguchi and Randall 2008). This estimate confirms that the diffusive contribution can dominate the entrainment process for low resolutions, resulting in an enhanced entrainment velocity.

Figure 9 shows that a high diffusive contribution introduces a scaling between t_{de} and κ for simulations made with the similar viscosity and cloud-top height (same t_0). If we assume that the desiccation time is commensurable with the cloud-breakup time [like suggested in, e.g., Yamaguchi and Randall (2008)], this scaling between t_{de} and κ would result in the known scaling of the cloud fraction versus κ for the cases in which the diffusive contribution dominates the entrainment. This might explain the good κ scaling found in some LES with grid spacings of the order of several meters.

b. Implication for entrainment models

In this section, we summarize the results that can be used to improve entrainment-velocity parameterizations. For this purpose, we use the general formula for entrainment velocity introduced by Stevens (2002):

$$w_e = \mathcal{U}\left(\frac{\mathcal{W}}{\Delta b}\right) + \mathcal{D}, \tag{25}$$

where the parameters $\mathcal{U}$, $\mathcal{W}$, and $\mathcal{D}$ are described below. We base our analysis on the integrated buoyancy equation [Eq. (22)], which is written in the form of Eq. (25) by using Eq. (14) in the limit of negligible deformation.

The parameter $\mathcal{W}$ quantifies the effect of the turbulence intensity on the entrainment. Stevens (2002) identifies $\mathcal{W}$ as the averaged integrated buoyancy flux in the CBL, although this definition might differ for other parameterizations. From Eq. (22) we identify $\mathcal{W}$ as the buoyancy flux at the inversion point F, and this term is analyzed in section 6a. Figure 7 shows that F is a constant fraction of the radiative forcing, and it is thus insensitive to the evaporative-cooling parameters in agreement with Moeng (2000). Contrary to the behavior of F, Table 1 shows that the averaged integrated buoyancy flux $\mathcal{B} = (z^*)^{-1}\int\langle w'b'\rangle\, dz$ can be enhanced by more than a factor of 2 when varying the evaporative-cooling parameters. We conclude that the assumption that $\mathcal{W}$ is a fraction of the averaged integrated buoyancy flux is not always correct. We also see that F does not scale either with the minimum turbulent flux (not shown). It remains to be investigated how F and $\mathcal{W}$ vary when other turbulence sources, as a surface buoyancy flux or shear, are also included.

The parameter $\mathcal{D}$, usually called direct cooling, quantifies the direct effect of the radiative cooling on the entrainment (Lilly 1968). It is considered as a nonturbulent contribution for the entrainment (Stevens 2002), although there is not a clear consensus in the literature about its magnitude and relevance (Wood 2012). Different parameterizations range from neglecting it (Turton and Nicholls 1987) to considering it the main contribution for the entrainment velocity (Lock and Mac Vean 1999). In our analysis, we identify the direct cooling with $S_{\text{rad}}^{\text{inv}}$, and this term is analyzed in section 6b. The extrapolation of $S_{\text{rad}}^{\text{inv}}$ to a 1-km-deep CBL in Fig. 8 indicates that the direct

cooling accounts for ~50% of the entrainment velocity. This quantification is broadly in agreement with the parameterizations of Lock (1998) and Moeng (2000).

The parameter $\mathcal{U}$ captures the entrainment-velocity dependence on the evaporative cooling. To obtain $\mathcal{U}$ from Eq. (22), it is necessary to make nontrivial assumptions about $S_{\mathrm{eva}}^{\mathrm{inv}}$, which do not necessarily lead to the form of the entrainment velocity proposed in Eq. (25) [as in, e.g., Lilly (2002)]. Although such a detailed analysis is beyond the scope of this paper, the sensitivity of $\mathcal{U}$ to the evaporative parameters is tested in an indirect way by comparing the entrainment velocity in the first set of experiments. Although the radiative-cooling parameters are the same in this set of experiments, we find that w_e varies by 100% when varying the evaporative-cooling parameter D. This result provides a rough estimate for the inaccuracies that can be expected when using a parameterization that neglects the evaporative cooling such as those of Lock (1998) and Moeng (2000).

The entrainment velocity is sensitive to both the radiative properties of the cloud (through $\mathcal{D}$) and the evaporative-cooling parameters (through $\mathcal{U}$). This dual dependence is not captured by most of current parameterizations, which implicitly assume that only one mechanism dominates the entrainment process. It becomes evident that a parameterization of the entrainment velocity that covers all stratocumulus regimes should consider both evaporative and radiative cooling in detail.

8. Conclusions

In this paper, we present a new formulation that allows us to identify the buoyancy sources due to radiative and evaporative cooling, while introducing only an error less than 3% in the buoyancy calculations for typical atmospheric conditions. The formulation is applied to investigate a shear-free cloud-top mixing layer driven by evaporative and radiative cooling with DNS. Our main findings are as follows:

- Our results do not converge as viscosity and grid spacing are reduced, even when the resolution is below 14 cm. The reason is that the BRI introduces a diffusive contribution that increases mixing by 20%. The enhancement of the mixing can be roughly predicted using the parameterization introduced by Mellado (2010), and it is much larger than 20% for resolutions commonly used in atmospheric simulations. This partially explains the rapid dessication of clouds and the κ criterion observed in LES. When the diffusive contribution is subtracted, our results for different viscosities collapse on top of each other. This inviscid scaling confirms that all small flow scales that are relevant for evaporative and radiative cooling are captured in our simulations, allowing us to make predictions for the atmospheric scales.
- The definition of the inversion point as the point of neutral buoyancy $[\langle b\rangle(z_i) = 0]$ allows us to derive two different scaling relationships in the cloud and entrainment zones. The in-cloud scaling law relates the velocity and buoyancy integral scales to a buoyancy flux defined by the inversion point. The entrainment scaling law provides a relationship between the entrainment velocity and the rate of evaporation of liquid water.
- The contributions from the buoyancy flux and the direct radiative cooling to the entrainment-zone cooling (which relates to the entrainment velocity) behave very similarly to the smoke case without evaporative cooling (De Lozar and Mellado 2013). The buoyancy flux is a constant fraction of the magnitude of the radiative flux divergence at the cloud top $F = (0.175 \pm 0.04)S_{\mathrm{rad}}$. This contribution is independent of the evaporative cooling and of the vertically averaged buoyancy flux. The buoyancy flux reaches this value when the CBL depth is around 4λ (~60 m), and it does not increase appreciably by the later growth of the CBL. This behavior strongly suggests that eddies that are larger than this size do not contribute directly to the entrainment. The direct radiative cooling accounts for around 50% of the buoyancy flux, and therefore cannot be neglected.
- The strength of evaporative and radiative cooling is quantified by their corresponding integrated inviscid buoyancy sources. Generally the strength of both mechanisms is of the same order of magnitude, and its ratio is close to one for the flight RF-01 of the DYCOMS-II campaign. This result, together with a detailed analysis of the integrated buoyancy equation, shows that entrainment-velocity parameterizations should consider both evaporative and radiative cooling and not just one or the other.

Acknowledgments. All data used for this study will be provided upon request to anyone interested. Support from the Max Planck Society through its Max Planck Research Groups program is gratefully acknowledged. We are grateful to Hermann Gerber and to the two anonymous reviewers, who helped to improve the manuscript. Computational time was provided by the Jülich Supercomputing Centre.

APPENDIX

Derivation of the Linearized Formulation

The starting point is the exact expression for the enthalpy and equation of state:

$$h = [c_{p,D}(1 - q_t) + c_{p,V}(q_t - q_l) + c_l q_l]T - q_l E \quad \text{and} \tag{A1}$$

$$p = \rho(1 - q_t)R_D T + \rho(q_t - q_l)R_V T, \tag{A2}$$

where E is the extrapolated latent heat to 0 K, $c_{p,D}$ and R_D are the specific heat capacity and gas constant of the dry phase, $c_{p,V}$ and R_V are the specific heat capacity and gas constant of the vapor phase, and c_l is the specific heat of the liquid phase. Using the Taylor expansion around a reference state given by (h^c, q_t^c, q_l^c), where the superscript c refers to a cloud value, allows us to write the buoyancy as

$$b/g = -\hat{\Delta}\rho/\rho = \hat{\Delta}h/(c_{p,0}T_c) + G_l\hat{\Delta}q_l + G_t\hat{\Delta}q_t, \tag{A3}$$

where the $\hat{\Delta}$ refers to the deviations of a variable from the reference value and the new constants are given by

$$\begin{aligned} G_l &= (E - c_l T_c)/(c_{p,0}T_c) + c_{p,V}/c_{p,0} - R_V/R_0, \\ G_t &= -(c_{p,V} - c_{p,D})/c_{p,0} + (R_V - R_D)/R_0, \\ c_{p,0} &= c_{p,D}(1 - q_t^c) + c_{p,V}(q_t^c - q_l^c), \quad \text{and} \\ R_0 &= (1 - q_t^c)R_D + \rho(q_t^c - q_l^c)R_V. \end{aligned} \tag{A4}$$

For a given (q_t, h) the only unknown in Eq. (A3) is the liquid water q_l. This can be calculated in the infinitely fast thermodynamics approximation, in which the liquid water is given by

$$\begin{aligned} q_l &= q_t - q_s \quad \text{if} \quad q_t > q_s \\ q_l &= 0 \quad \text{if} \quad q_t < q_s \end{aligned}. \tag{A5}$$

The saturated vapor content q_s is given by

$$q_s = p_s(T)\frac{(1 - q_t)R_D}{[p - p_s(T)]R_V}, \tag{A6}$$

where $p_s(T)$ is the water saturation pressure, which is a function of the temperature only. We calculate $p_s(T)$ using the polynomial expression given by Flatau et al. (1992). Equation (A6) can be approximated by the first-order Taylor expansion:

$$q_s = q_s^c + \gamma_h\hat{\Delta}h/(c_{p,0}T_c) + \gamma_{q_t}\hat{\Delta}q_t, \tag{A7}$$

with the derivatives

$$\begin{aligned} \gamma_h &= c_{p,0}T_c(\partial q_s/\partial h)_{q_t} \quad \text{and} \\ \gamma_{q_t} &= (\partial q_s/\partial q_t)_h, \end{aligned} \tag{A8}$$

which are calculated at the reference state, which we choose to contain nonzero liquid water. Since the γ derivatives are calculated for saturated conditions, the linear approximation for q_s does not apply for unsaturated parcels. However, the formulation never makes use of q_s in the unsaturated parcels, thus justifying the linear approximation. Using Eq. (A7) in Eq. (A5) together with Eqs. (1) and (2), we obtain the piecewise linear expression for the liquid water and buoyancy introduced in Eq. (5).

The γ derivatives are calculated in its exact form by using the chain rule. The term γ_h is given by

$$\gamma_h/c_{p,0}T_c = \frac{(\partial q_s/\partial p_s)_{q_t,h}(\partial p_s/\partial T)_{q_t,h}(\partial T/\partial h)_{q_t,q_s}}{1 - (\partial q_s/\partial p_s)_{q_t,h}(\partial p_s/\partial T)_{q_t,h}(\partial T/\partial q_s)_{q_t}}, \tag{A9}$$

with

$$\begin{aligned} (\partial q_s/\partial p_s)_{q_t,h} &= \frac{q_s}{(1 - p_s/p)p_s}, \\ (\partial T/\partial h)_{q_t,q_s} &= \frac{1}{c_{p,0}}, \quad \text{and} \\ (\partial T/\partial q_s)_{q_t,h} &= -\frac{E + (c_{p,V} - c_l)T_c}{c_{p,0}}, \end{aligned} \tag{A10}$$

and γ_{q_t} is given by

$$\gamma_{q_t} = \frac{(\partial q_s/\partial q_t)_{p_s,h} + (\partial q_s/\partial p_s)_{h,q_t}(\partial p_s/\partial T)_{q_t,h}(\partial T/\partial q_t)_{h,q_s}}{1 - (\partial q_s/\partial p_s)_{h,q_t}(\partial p_s/\partial T)_{q_t,h}(\partial T/\partial q_s)_{h,q_t}}, \tag{A11}$$

with

$$(\partial q_s/\partial q_t)_{p_s,h} = \frac{-R_D}{(p/p_s - 1)R_V} \quad \text{and} \tag{A12}$$

$$(\partial T/\partial q_t)_{h,q_s} = \frac{E + (c_{p,D} - c_l)T_c}{c_{p,0}}. \tag{A13}$$

The derivative $(\partial p_s/\partial T)_{q_t,h}$ is obtained from the parameterization given by Flatau et al. (1992).

Algebraical manipulations allow us to obtain the nondimensional parameters introduced in Eqs. (5)–(6) from the parameters presented in this appendix:

$$\begin{aligned} \chi_s &= q_l^c[\gamma_h\Delta h/(c_{p,0}T_c) - \Delta q_t(1 - \gamma_{q_t})]^{-1}, \\ D &= \frac{-\chi_s g}{\Delta b}\left\{\frac{\Delta h}{c_{p,0}T_c}(1 - G_l\gamma_h) + \Delta q_t[G_t + G_l(1 - \gamma_{q_t})]\right\}, \\ \beta &= 1 - G_l\gamma_h, \\ \psi_b &= (c_{p,0}T_c\Delta b)g^{-1}, \quad \text{and} \\ \psi_s &= \psi_b(D + \chi_s)(1 - \chi_s)^{-1}(1 - \beta)^{-1}, \end{aligned} \tag{A14}$$

where the Δ symbol represents the difference between the dry and cloud states that characterize a mixing layer. The parameters ψ_b and ψ_s scale how the changes in enthalpy by radiation, given by ψ in Eq. (2), modify the nondimensional buoyancy and liquid water, respectively.

REFERENCES

Albrecht, B. A., R. S. Penc, and W. H. Schubert, 1985: An observational study of cloud-topped mixed layers. *J. Atmos. Sci.*, **42**, 800–822, doi:10.1175/1520-0469(1985)042<0800:AOSOCT>2.0.CO;2.

Bretherton, C. S., 1987: A theory for nonprecipitating moist convection between two parallel plates. Part I: Thermodynamics and "linear" solutions. *J. Atmos. Sci.*, **44**, 1809–1827, doi:10.1175/1520-0469(1987)044<1809:ATFNMC>2.0.CO;2.

——, and Coauthors, 1999: An intercomparison of radiatively driven entrainment and turbulence in a smoke cloud, as simulated by different numerical models. *Quart. J. Roy. Meteor. Soc.*, **125**, 391–423, doi:10.1002/qj.49712555402.

Carpenter, M. H., and C. A. Kennedy, 1994: Fourth-order 2N-storage Runge-Kutta schemes. NASA Langley Research Center Tech. Memo. 109112, 24 pp. [Available online at http://www.ece.uvic.ca/~bctill/papers/numacoust/Carpenter_Kennedy_1994.pdf.]

Deardorff, J. W., 1970: Convective velocity and temperature scales for the unstable planetary boundary layer and for Rayleigh convection. *J. Atmos. Sci.*, **27**, 1211–1213, doi:10.1175/1520-0469(1970)027<1211:CVATSF>2.0.CO;2.

——, 1980: Cloud top entrainment instability. *J. Atmos. Sci.*, **37**, 131–147, doi:10.1175/1520-0469(1980)037<0131:CTEI>2.0.CO;2.

De Lozar, A., and J. P. Mellado, 2013: Direct numerical simulations of a smoke cloud-top mixing layer as a model for stratocumuli. *J. Atmos. Sci.*, **70**, 2356–2375, doi:10.1175/JAS-D-12-0333.1.

——, and ——, 2014: Cloud droplets in a bulk formulation and its application to buoyancy reversal instability. *Quart. J. Roy. Meteor. Soc.*, **140**, 1493–1504, doi:10.1002/qj.2234.

Dimotakis, P. E., 2005: Turbulent mixing in stratified fluids. *Annu. Rev. Fluid Mech.*, **37**, 329–356, doi:10.1146/annurev.fluid.36.050802.122015.

Faloona, I., and Coauthors, 2005: Observations of entrainment in eastern Pacific marine stratocumulus using three conserved scalars. *J. Atmos. Sci.*, **62**, 3268–3285, doi:10.1175/JAS3541.1.

Fernando, H. J. S., 1991: Turbulent mixing in stratified fluids. *Annu. Rev. Fluid Mech.*, **23**, 455–493, doi:10.1146/annurev.fl.23.010191.002323.

Flatau, P. J., R. L. Walko, and W. R. Cotton, 1992: Polynomial fits to saturation vapor pressure. *J. Appl. Meteor.*, **31**, 1507–1513, doi:10.1175/1520-0450(1992)031<1507:PFTSVP>2.0.CO;2.

Gerber, H., G. Frick, S. P. Malinowski, H. Jonsson, D. Khelif, and S. K. Krueger, 2013: Entrainment rates and microphysics in POST stratocumulus. *J. Geophys. Res. Atmos.*, **118**, 12 094–12 109, doi:10.1002/jgrd.50878.

Haman, K. E., 2009: Simple approach to dynamics of entrainment interface layers and cloud holes in stratocumulus clouds. *Quart. J. Roy. Meteor. Soc.*, **135**, 93–100, doi:10.1002/qj.363.

Katzwinkel, J., H. Siebert, and R. A. Shaw, 2012: Observation of a self-limiting, shear-induced turbulent inversion layer above marine stratocumulus. *Bound.-Layer Meteor.*, **145**, 131–143, doi:10.1007/s10546-011-9683-4.

Klingebiel, M., and Coauthors, 2015: Arctic low-level boundary layer clouds: In-situ measurements and simulations of mono- and bimodal supercooled droplet size distributions at the cloud top layer. *Atmos. Chem. Phys.*, **15**, 617–631, doi:10.5194/acp-15-617-2015.

Larson, V. E., K. E. Kotenberg, and N. B. Wood, 2007: An analytic longwave radiation formula for liquid layer clouds. *Mon. Wea. Rev.*, **135**, 689–699, doi:10.1175/MWR3315.1.

Lele, S. K., 1992: Compact finite difference schemes with spectral-like resolution. *J. Comput. Phys.*, **103**, 16–42, doi:10.1016/0021-9991(92)90324-R.

Lilly, D. K., 1968: Models of cloud-topped mixed layers under a strong inversion. *Quart. J. Roy. Meteor. Soc.*, **94**, 292–309, doi:10.1002/qj.49709440106.

——, 2002: Entrainment into mixed layers. Part II: A new closure. *J. Atmos. Sci.*, **59**, 3353–3361, doi:10.1175/1520-0469(2002)059<3353:EIMLPI>2.0.CO;2.

Lock, A., 1998: The parametrization of entrainment in cloudy boundary layers. *Quart. J. Roy. Meteor. Soc.*, **124**, 2729–2753, doi:10.1002/qj.49712455210.

——, 2009: Factors influencing cloud area at the capping inversion for shallow cumulus clouds. *Quart. J. Roy. Meteor. Soc.*, **135**, 941–952, doi:10.1002/qj.424.

——, and M. K. Mac Vean, 1999: The parametrization of entrainment driven by surface heating and cloud-top cooling. *Quart. J. Roy. Meteor. Soc.*, **125**, 271–299, doi:10.1002/qj.49712555315.

Mellado, J. P., 2010: The evaporatively driven cloud–top mixing layer. *J. Fluid Mech.*, **660**, 5–36, doi:10.1017/S0022112010002831.

——, 2012: Direct numerical simulation of free convection over a heated plate. *J. Fluid Mech.*, **712**, 418–450, doi:10.1017/jfm.2012.428.

——, and C. Ansorge, 2012: Factorization of the Fourier transform of the pressure-Poisson equation using finite differences in colocated grids. *Z. Angew. Math. Mech.*, **92**, 380–392, doi:10.1002/zamm.201100078.

——, B. Stevens, H. Schmidt, and N. Peters, 2009: Buoyancy reversal in cloud-top mixing layers. *Quart. J. Roy. Meteor. Soc.*, **135**, 963–978, doi:10.1002/qj.417.

——, ——, ——, and ——, 2010: Two-fluid formulation of the cloud-top mixing layer for direct numerical simulation. *Theor. Comput. Fluid Dyn.*, **24**, 511–536, doi:10.1007/s00162-010-0182-x.

——, ——, and ——, 2014: Wind shear and buoyancy reversal at the top of stratocumulus. *J. Atmos. Sci.*, **71**, 1040–1057, doi:10.1175/JAS-D-13-0189.1.

Moeng, C., 2000: Entrainment rate, cloud fraction, and liquid water path of PBL stratocumulus clouds. *J. Atmos. Sci.*, **57**, 3627–3643, doi:10.1175/1520-0469(2000)057<3627:ERCFAL>2.0.CO;2.

Monin, A. S., and A. M. Yaglom, 1971: *Mechanics of Turbulence*. Vol. 1, *Statistical Fluid Mechanics*, MIT Press, 782 pp.

Patankar, S. V., 1980: *Numerical Heat Transfer and Fluid Flow*. Hemisphere Series on Computational Methods in Mechanics and Thermal Science, CRC Press, 214 pp.

Pauluis, O., and J. Schumacher, 2010: Idealized moist Rayleigh-Benard convection with piecewise linear equation of state. *Commun. Math. Sci.*, **8**, 295–319, doi:10.4310/CMS.2010.v8.n1.a15.

Pope, S. B., 2000: *Turbulent Flows*. Cambridge University Press, 802 pp.

Randall, D. A., 1980: Conditional instability of the first kind upside-down. *J. Atmos. Sci.*, **37**, 125–130, doi:10.1175/1520-0469(1980)037<0125:CIOTFK>2.0.CO;2.

Sandu, I., and B. Stevens, 2011: On the factors modulating the stratocumulus to cumulus transitions. *J. Atmos. Sci.*, **68**, 1865–1881, doi:10.1175/2011JAS3614.1.

Siems, S. T., and C. S. Bretherton, 1992: A numerical investigation of cloud-top entrainment instability and related experiments. *Quart. J. Roy. Meteor. Soc.*, **118**, 787–818, doi:10.1002/qj.49711850702.

Stevens, B., 2002: Entrainment in stratocumulus-topped mixed layers. *Quart. J. Roy. Meteor. Soc.*, **128**, 2663–2690, doi:10.1256/qj.01.202.

——, 2005: Atmospheric moist convection. *Annu. Rev. Earth Planet. Sci.*, **33**, 605–643, doi:10.1146/annurev.earth.33.092203.122658.

——, and Coauthors, 2005: Evaluation of large-eddy simulations via observations of nocturnal marine stratocumulus. *Mon. Wea. Rev.*, **133**, 1443–1462, doi:10.1175/MWR2930.1.

Turton, J., and S. Nicholls, 1987: A study of the diurnal variation of stratocumulus using a multiple mixed layer model. *Quart. J. Roy. Meteor. Soc.*, **113**, 969–1009, doi:10.1002/qj.49711347712.

van der Dussen, J. J., S. R. de Roode, and A. P. Siebesma, 2014: Factors controlling rapid stratocumulus cloud thinning. *J. Atmos. Sci.*, **71**, 655–664, doi:10.1175/JAS-D-13-0114.1.

van Zanten, M. C., and P. G. Duynkerke, 2002: Radiative and evaporative cooling in the entrainment zone of stratocumulus—The role of longwave radiative cooling above cloud top. *Bound.-Layer Meteor.*, **102**, 253–280, doi:10.1023/A:1013129713315.

Wood, R., 2012: Stratocumulus clouds. *Mon. Wea. Rev.*, **140**, 2373–2423, doi:10.1175/MWR-D-11-00121.1.

Yamaguchi, T., and D. A. Randall, 2008: Large-eddy simulation of evaporatively driven entrainment in cloud-topped mixed layers. *J. Atmos. Sci.*, **65**, 1481–1504, doi:10.1175/2007JAS2438.1.

——, and ——, 2012: Cooling of entrained parcels in a large-eddy simulation. *J. Atmos. Sci.*, **69**, 1118–1136, doi:10.1175/JAS-D-11-080.1.

Yue, Q., B. H. Kahn, H. Xiao, M. M. Schreier, E. J. Fetzer, J. Teixeira, and K. Suselj, 2013: Transitions of cloud-topped marine boundary layers characterized by AIRS, MODIS, and a large eddy simulation model. *J. Geophys. Res. Atmos.*, **118**, 8598–8611, doi:10.1002/jgrd.50676.